Chemical Engineering Journal 483 (2024) 149289

Contents lists available at ScienceDirect

Chemical Engineering Journal

journal homepage: www.elsevier.com/locate/cej

Exfoliated misfit layer compounds synergize conversion-alloying-intercalation triple mechanism for enhanced rate performance in potassium ion storages

Shou-Shan Mai, Yi-Chun Yang, Hsing-Yu Tuan *

Department of Chemical Engineering, National Tsing Hua University, Hsinchu 30013, Taiwan

ARTICLE INFO

Keywords:
Misfit layered compound
Few-layer
Hybrid capacitor
High rate
Potassium ion

ABSTRACT

Misfit layer compounds (MLC) exhibit a distinctive alternating stacking structure, fostering mismatched heterointerfaces that synergistically enhance interface charge storage and electrode structural integrity. In this study, we synthesized exfoliated few-layer $(BiSe)_{1.10}NbSe_2$ MLC (FL-$(BiSe)_{1.10}NbSe_2$ MLC) through vacuum solid-state synthesis complemented by point probe ultrasonic processing. By strategically alternating BiSe and $NbSe_2$ layers, a structured stack with a naturally mismatched heterogeneous interface is achieved. This design leverages a threefold mechanism involving conversion, alloying, and intercalation, contributing to enhanced electrochemical stability of the material. Finite element analysis reveals that the FL-$(BiSe)_{1.10}NbSe_2$ exhibits reduced interfacial stress compared to pure BiSe, ensuring superior structural integrity of BiSe within the $NbSe_2$ layers. Utilizing the van der Waals gaps within $NbSe_2$ layers for improved K^+ migration, the MLC exhibits remarkable rate performance, representing its first successful integration into potassium ion hybrid capacitor (PIHC) components. Consequently, the FL-$(BiSe)_{1.10}NbSe_2$ electrode, serving as the potassium-ion battery (PIB) anode shows a capacity of 191 mA h g^{-1} at 4 A/g with consistent cyclability, enduring 2000 cycles at a 1 A/g current density in the PIHC configuration. This study provides new insights into the structural strategy for electrodes with conversion, alloying, and intercalation triple mechanisms, in addition to offering a reliable pathway for designing carbon-free potassium-ion intercalation anode materials.

1. Introduction

Given the challenges posed by the depletion of lithium resources, characterized by a scarcity rate of 0.0017 % and a concentrated distribution with South America accounting for 70 %, there is an escalating concern regarding cost implications. In this context, potassium-ion batteries (PIBs) emerge as a promising alternative for the next generation of rechargeable batteries, presenting a compelling option for energy storage systems [1–3]. A significant challenge with PIBs arises from the larger atomic radius of potassium ions (K^+ with a radius of 0.138 nm) compared to lithium ions (Li^+ with a radius of 0.076 nm). The size difference diminishes K^+ mobility in solid states, impeding their movement within the host material. As the host material interacts with negatively charged ions, it undergoes pronounced volume expansion, reducing the electrode's integrity and leading to a decline in the capacity and energy density of PIBs. Widely used carbon-based anode materials like graphite offer benefits in conductivity, cost, and abundance [4–7]. However, the limited capacity due to low K^+ insertion (e.g., KC_8 in PIBs) poses challenges, prompting a focus on developing non-carbon electrodes for improved potassium-ion storage [8].

Two-dimensional (2D) conversion materials [9–12] derived from layered compounds, are advantageous in evenly dispersing internal stress during the K^+ insertion/extraction process. Their inherent 2D structure effectively alleviates mechanical stress, preventing electrode degradation [13]. Moreover, due to their expansive surface area compared to other materials, 2D structures facilitate superior contact with the electrolyte, leading to a more homogeneous charge distribution beneficial for K^+ adsorption [14,15]. Within the category of 2D conversion materials, transition metal dichalcogenides (TMDCs) are particularly noteworthy for their distinct interlayer spacing [16–19], impressive theoretical storage capacity, tunable interlayer distances, and intrinsic high conductivity. These attributes collectively expedite ion transport, enhancing ion migration speed and reducing the energy thresholds for intercalation reactions, offering an optimal landscape for

* Corresponding author.
E-mail address: hytuan@che.nthu.edu.tw (H.-Y. Tuan).

https://doi.org/10.1016/j.cej.2024.149289
Received 3 November 2023; Received in revised form 12 January 2024; Accepted 31 January 2024
Available online 3 February 2024

swift K^+ intercalation/deintercalation. For example, 1 T′-phase WS_2 nanosheets allow control over thickness and improve Li^+ storage in TMDC nanosheets. $NbSe_2$, a prototypical TMDC, is notable for its exceptional conductivity, measured at 6.7×10^3 S cm^{-1} [20], and high bulk modulus of 114 GPa [21], making it highly sought after in energy storage applications. For instance, Subramanian et al. synthesized a layered $NbSe_2$ structure as an anode material for sodium-ion hybrid capacitors through a gas-phase solid-state reaction. They achieved an impressive 93.2 % retention of their initial capacity after 3,000 cycles at a current rate of 300 mA g^{-1} [22]. Similarly, Carrasco et al. employed aqueous electrochemical exfoliation to produce $NbSe_2$ nanosheets/nanorolls, resulting in elevated Li^+ storage capacities [23]. However, the van der Waals (vdW) forces in TMDCs can lead to layer re-stacking, reducing surface area and impairing ion diffusion, which hinders K^+ transport and degrades electrochemical performance [24].

Misfit layer compounds (MLC) have recently gained attention due to their distinct atomic arrangement, characterized by a unique alternating layered stacking structure [25]. These materials follow the formula $(MX)_{1+a}(TX_2)_b$; MX refers to a monochalcogenide layer, including elements like Sn, Pb, Bi, Sb, and rare earths, with TX_2 representing a TMDC layer, where X can be S, Se, or Te. The variable b represents the number of TMDC layers before each MX layer, and the misfit index a, ranging from 0.08 to 0.28, indicates the degree of layer incongruity, whose estimate comes from ionic radii [26,27]. Recent investigations into MLC include $(LaSe)_{1.14}(NbSe_2)_2$ using various techniques, revealing the adjustable nature of its layers [28]. Nader et al. studied the magnetic field's temperature dependency for $(BiSe)_{1.10}NbSe_2$ and $(BiS)_{1.11}NbS_2$, suggesting their potential as anisotropic 3D superconductors [29]. Muhammad et al. highlighted the thermoelectric properties of BSC-222 misfit layered oxide materials for supercapacitor applications [30]. Zullo et al. confirmed superconductivity in $(LaSe)_{1.27}(SnSe_2)_2$, hinting at its potential in field-effect transistors [28]. The vdW bond between MX and TX_2 creates a natural heterojunction, enhancing mechanical properties capable of countering volume fluctuations. As a result, $NbSe_2$-based MLC are gaining attraction as potential anode materials in energy storage [27].

Herein, we introduce FL-$(BiSe)_{1.10}NbSe_2$ MLC anode for PIBs. BiSe and $NbSe_2$ synthesized via a vacuum solid-phase method are modulated to minimize interlayer repulsion and induce ordered stacking. Within $(BiSe)_{1.10}NbSe_2$, there exists a vdW gap between adjacent $NbSe_2$ layers. Consequently, layer-by-layer exfoliation is achieved through point probe ultrasonication, yielding exceptional thin flakes by selectively delaminating individual $NbSe_2$ vdW gaps. The unique interlayer structure inherent in $NbSe_2$-based MLC provides a robust and highly conductive scaffold for the fragile and poorly conductive BiSe. This distinctive MLC material, characterized by its unique structure and properties, offers K^+ a novel migration pathway that enables a conversion-alloying-intercalation triple mechanism, further enhancing K^+ diffusion rates. As a result, FL-$(BiSe)_{1.10}NbSe_2$ exhibits several advantages over pristine BiSe, including excellent reversibility, notable pseudo-capacitive contributions, reduced charge transfer resistance (Rct) values, higher diffusion coefficients, and improved rate capabilities.

2. Experimental section

2.1. Materials

Niobium powder, bismuth powder were purchased from Alfa Aesar. Selenium powder, potassium metal, and anhydrous dimethyl carbonate were obtained from Sigma-Aldrich, while potassium bis(fluorosulfonyl) imide was acquired from Combi-Blocks. We purchased sodium carboxymethyl cellulose (NaCMC), Super-P, and coin-type cell CR2032 from Shining Energy, and glass fiber from Advantec. Additionally, aluminum and copper foil were procured from the Chang-Chun group. All chemicals were used as received without additional purification.

2.2. Material characterization

We examined the morphologies of all materials using various techniques, including scanning electron microscopy (SEM, HITACHI-SU8010), atomic force microscopy (AFM, Veeco DI-3100, NCHU), transmission electron microscopy (TEM), selected-area electron diffraction (SAED), and high-angle annular dark-field (HAADF) imaging (JEOL, JEM-ARM200FT, NTHU). We also carried out X-ray photoelectron spectroscopy (XPS) analysis (XPSPEAK VER. 4.1 software), X-ray diffraction (XRD) using a Bruker D8 ADVANCE instrument with Cu-Kα radiation ($\lambda = 1.54$ Å), and high-resolution XPS using ULVAC-PH's PHI QuanteraII instrument at NTHU.

2.3. Synthesis of bulk $NbSe_2$, BiSe, $(BiSe)_{1.10}NbSe_2$

Bulk $NbSe_2$, BiSe, and $(BiSe)_{1.10}NbSe_2$ were synthesized by solid-state reaction with a total mass of 250 mg nominal composition powders. Nb, Bi and Se powders were sealed in a vacuum quartz tube with the stoichiometric molar ratio, and the sealed tube was put into the tube furnace. For $NbSe_2$, BiSe and $(BiSe)_{1.10}NbSe_2$, the tube was heated at 10 °C min^{-1} and kept at 750 °C for 24 h. After the solid sintering process, bulk $NbSe_2$, BiSe, and $(BiSe)_{1.10}NbSe_2$ were obtained.

2.4. Synthesis of FL-$(BiSe)_{1.10}NbSe_2$

After fully grounding $(BiSe)_{1.10}NbSe_2$in an agate mortar, 100 mg powder was added into a sample tube containing 25 mL deionized water. The mixture underwent point probe sonication at 125 W and 20 kHz for 4 h, and the entire procedure was conducted while maintaining a cooling system with ice. Finally, FL-$(BiSe)_{1.10}NbSe_2$ was obtained through centrifugation, followed by multiple washes using deionized water and ethanol. The resulting material was then dried overnight at 60 °C.

2.5. Electrochemical measurement

A coin-type half-cell (CR2032) was meticulously assembled within a glovebox (filled with argon gas) for electrochemical testing. An evenly mixed slurry of the anode material was prepared by combining the active material, super P, and NaCMC in a ratio of 7:2:1 in deionized water. The resulting slurry was coated with copper foil and dried at 80 °C under an argon atmosphere. Each electrode exhibited an average material mass loading range from 0.9 to 1.1 mg cm^{-2}. Glass fiber and a Celgard 2400 membrane were used as the separator in the half-cell setup, while a potassium metal foil functioned as the counter electrode. The electrolyte consisted of a 1 M KFSI solution in DMC (~200 μL per cell). Galvanostatic discharge/charge tests were conducted within 0.01 V to 3 V using a Neware battery analyzer (Neware, China). Electrochemical impedance spectroscopy (EIS) and cyclic voltammetry (CV) data were recorded with a multi-channel electrochemical analyzer (Bio-Logic-Science Instruments, VMP3). Additionally, the galvanostatic intermittent titration technique (GITT) involved charging and discharging at a current density of 50 mA g^{-1} for 10 min, with a relaxation time of 1 h, utilizing the Maccor Series 4000 battery test system.

2.6. Potassium-ion hybrid capacitor (PIHC) of FL-$(BiSe)_{1.10}NbSe_2$//AC

The PIHC was constructed with FL-$(BiSe)_{1.10}NbSe_2$ as the anode material and active carbon as the cathode material, in a mass ratio of 1:1.2. Before assemblingthe hybrid capacitor, the anode underwent preactivation through 20 cycles of discharge down to 0.01 V. Subsequently, we utilized 1 M KFSI in DMC as the electrolyte and defined the operational voltage range of the hybrid capacitor as 0.05 V to 3.8 V.

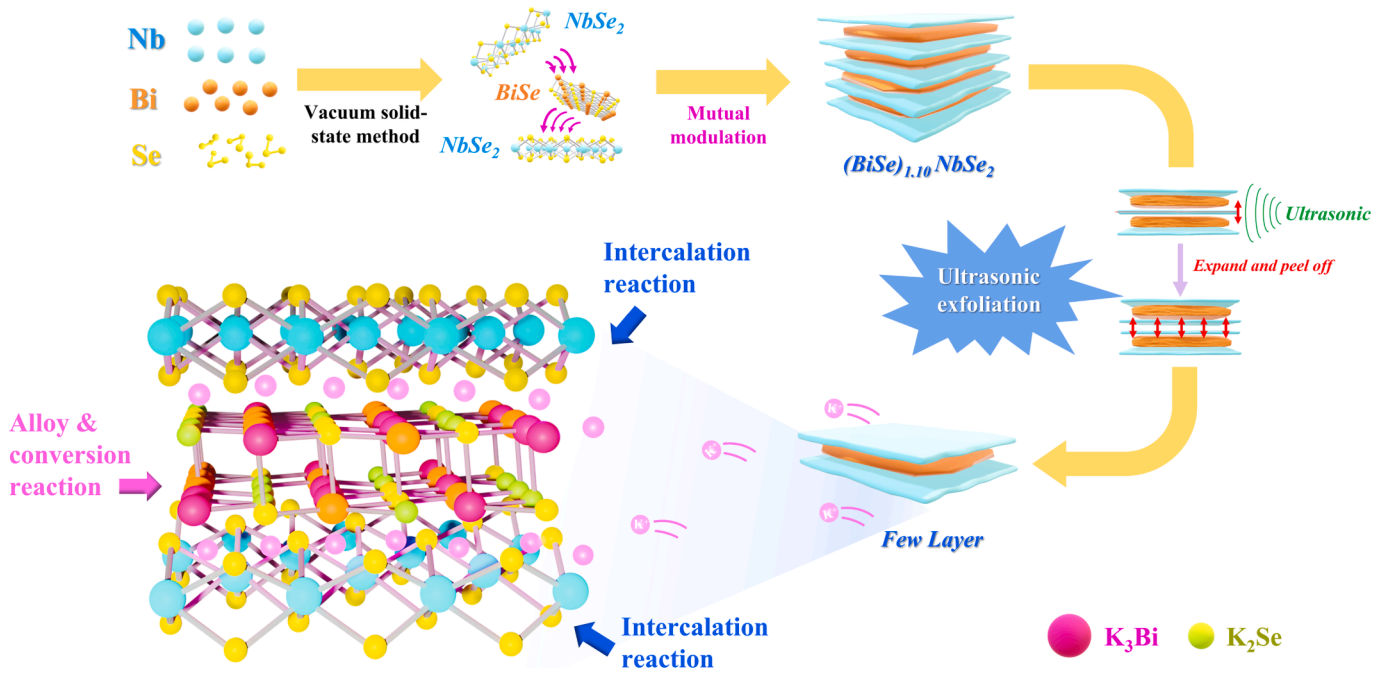

Fig. 1. Schematic illustration of synthetic route and crystal structure with K^+ transfer direction of FL-$(BiSe)_{1.10}NbSe_2$ MLC interface defect engineering.

2.7. Finite element analysis (FEA) simulation

We used a perfectly elastic–plastic model to characterize the deformation induced by potentiation and applied a nonlinear diffusion model to simulate the particle diffusion process. All simulation, pre-processing, and post-processing tasks were executed using COMSOL 6.1. Due to the analogous nature of the governing equations for thermal and mass diffusion, we opted to substitute COMSOL's diffusion and stress–strain fields with the temperature-displacement coupling program. Within our model, we substituted the thermal expansion coefficient for the expansion coefficient βij and the temperature field for the normalized K^+ concentration. It was assumed that the volume of $(BiSe)_{1.10}NbSe_2$ increases by 223 % after complete diffusion. The volume expansion coefficient for BiSe was set at $\beta_{ij} = 1.9 \times 10^{-5}$ [31], and for $NbSe_2$, at $\beta_{ij} = 6.6 \times 10^{-6}\ K^{-1}$ [32]. Under ideal conditions, $NbSe_2$ acted as the outer boundary, maintaining uniform K_3Bi, K_2Se, $K_{0.67}NbSe_2$, constant Poisson's ratio and elastic modulus. This configuration provided mechanical support for the confinement of $(BiSe)_{1.10}NbSe_2$.

3. Results and discussion

As shown in Fig. 1, the manufacturing process of FL-$(BiSe)_{1.10}NbSe_2$ primarily consists of several stages. Initially, BiSe and $NbSe_2$ are synthesized through a straightforward vacuum solid-phase method, and a vacuum quartz tube is employed for the mutual modulation, leading to an ordered and balanced stacking of $(BiSe)_{1.10}NbSe_2$. Subsequent ultrasonic treatment with a point probe enlarges the vdW gaps between $(BiSe)_{1.10}NbSe_2$, achieving a layered exfoliation effect, resulting in the formation of the extremely thin FL-$(BiSe)_{1.10}NbSe_2$. FL-$(BiSe)_{1.10}NbSe_2$ possesses a unique layered and alternately stacked structure [27]. The synergy between different characteristic components, such as $NbSe_2$ and BiSe, creates a naturally misfitted heterojunction, leading to a cooperative effect. The FL-$(BiSe)_{1.10}NbSe_2$ MLC material, with its distinctive structure and properties, offers new pathways for K^+, making it easier for K^+ to undergo conversion-alloying reactions with BiSe to generate K_3Bi and K_2Se. Additionally, its improved mechanical properties effectively mitigate volume changes during potassium insertion/extraction, thus significantly enhancing K^+ storage performance during potassium cycling. By merging BiSe's conversion-alloying with $NbSe_2$'s intercalation reactions [33,34,25,35], FL-$(BiSe)_{1.10}NbSe_2$ material was developed, featuring three mechanisms: conversion, alloying, and intercalation. This anode offers a triple-capacity contribution from these processes. As a result, it offers a significantly higher specific capacity compared to materials relying solely on the alloying mechanism or conversion reaction. Furthermore, the alloying reaction effectively reduces the average working voltage of the electrode. Finally, the MLC structure acts as a buffer zone for the substantial stress caused by the volume expansion during the conversion-alloying reaction, enhancing the mechanical stability of the electrode material and maintaining its structural integrity. The synergistic effect resulting from the combination of BiSe and $NbSe_2$ also enhances the potassium storage pseudocapacitive performance.

XRD analysis of the synthesized product yields a unique diffraction pattern, consistent with a misfit phase of $(BiSe)_{1.10}NbSe_2$, BiSe, and $NbSe_2$ (as depicted in Fig. 2a, S1). This pattern suggests the coexistence of hexagonal BiSe (P-3m1 (1 6 4), JCPDS No. 04-011-5568) and hexagonal $NbSe_2$ (P63/mmc (1 9 4), JCPDS No. 04-007-0992). The observed diffraction peak corresponding to $BiNbSe_3$ (JCPDS No. 00-046-1025) is attributable to the misfit phase $(BiSe)_{1.10}NbSe_2$ [36,37], which reveals a combination of the individual diffraction peaks of BiSe and $NbSe_2$ obtained via the burnt tube method. Subsequently, the weak interlayer adhesion in $(BiSe)_{1.10}NbSe_2$ facilitates the inclusion of solvent molecules, thereby expanding layer spacing and enhancing both capacitance and rate performance. FESEM was employed to investigate the morphology and microstructure of FL-$(BiSe)_{1.10}NbSe_2$, BiSe, and $NbSe_2$ (Fig. 2b-c, S2-4). After a post-ultrasonic treatment, this phase transitioned into a well-layered structure with an average particle size of 500 nm. AFM measurements, represented in Fig. 2d and Fig. 2e, revealed a single flake thickness of approximately 5 nm for FL-$(BiSe)_{1.10}NbSe_2$, thus affirming its successful synthesis. Fig. S5a-f discloses that $(BiSe)_{1.10}NbSe_2$ and $NbSe_2$ display a thickness range of 15–40 nm, while pure BiSe exhibits a notably greater thickness (~120 nm), thereby substantiating the comparative thinness of FL-$(BiSe)_{1.10}NbSe_2$. High-resolution XPS analyses were performed on FL-$(BiSe)_{1.10}NbSe_2$ (Fig. 2f-h, S7a), as well as on control samples of pure BiSe and $NbSe_2$ (Figs. S6, S7b-c). As illustrated in Fig. 2f, the Bi-4f spectrum of FL-$(BiSe)_{1.10}NbSe_2$ contains four peaks, two of which at 158.4 eV and 163.7 eV correspond to Bi-$4f_{7/2}$ and Bi-$4f_{5/2}$ states [38], respectively. The

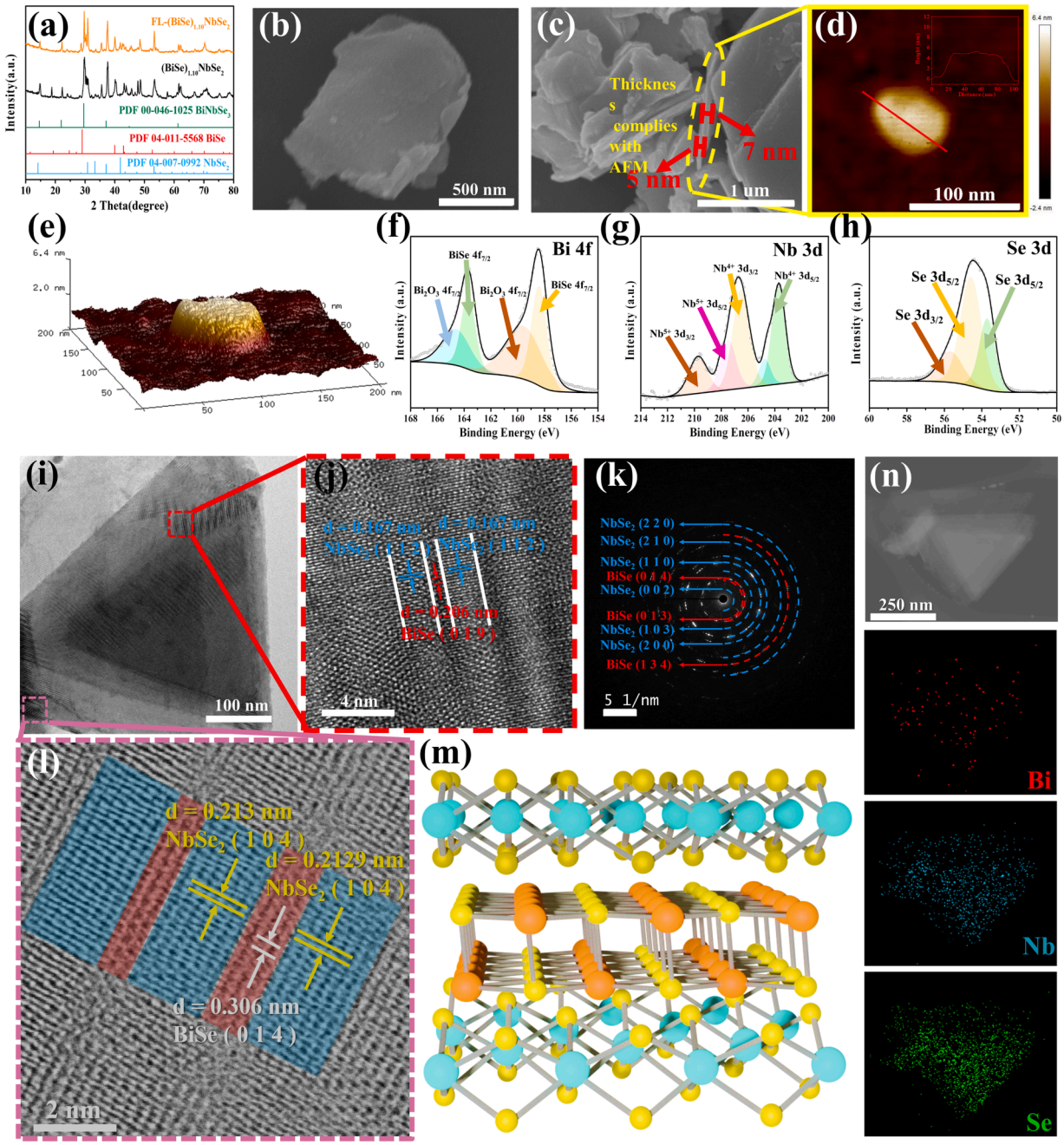

Fig. 2. (a) XRD patterns of FL-$(BiSe)_{1.10}NbSe_2$ MLC and $(BiSe)_{1.10}NbSe_2$, (b,c) SEM images of FL-$(BiSe)_{1.10}NbSe_2$, (d,e) AFM characterizations of FL-$(BiSe)_{1.10}NbSe_2$, (f) XPS spectrum of Bi 4f, (g) Nb 3d, and (h) Se 3d region of FL-$(BiSe)_{1.10}NbSe_2$, (i) TEM image, (j) HRTEM image, (k) SAED pattern, (l) HAADF-STEM images of FL-$(BiSe)_{1.10}NbSe_2$, (m) crystal structure of FL-$(BiSe)_{1.10}NbSe_2$ (n) EDS mapping images of MLC FL-$(BiSe)_{1.10}NbSe_2$ and corresponding elements of Bi, Nb, and Se.

other two peaks at 159.7 eV and 164.7 eV are attributed to bismuth oxide [39,40]. The Nb 3d spectrum of FL-$(BiSe)_{1.10}NbSe_2$ (Fig. 2g) comprises four distinct peaks. Peaks at 206.5 eV and 203.7 eV correspond to $Nb^{4+}3d_{3/2}$ and $Nb^{4+}3d_{5/2}$ in $NbSe_2$, aligning well with previous literature [41,42]. In addition, the small peaks centered at 207.5 eV (Nb^{5+} $3d_{5/2}$) and 209.8 eV (Nb^{5+} $3d_{3/2}$) can be indexed to Nb_2O_5 due to the oxidation on the surface [43]. The Se 3d spectrum features three peaks at 54.6, 53.7, and 55.7 eV, attributable to a blend of BiSe and $NbSe_2$ compositions (Fig. 2h).

Also, the particle size was determined by low-magnification TEM (Fig. 2i), consistent with high-resolution TEM (HRTEM) findings (Fig. 2j). HRTEM images delineate alternating layers of $NbSe_2$ and BiSe, confirming the misfit phase structure in $(BiSe)_{1.10}NbSe_2$ [25,36]. SAED confirmed the multiphasic nature (Fig. 2k), while HAADF-STEM revealed lattice stripe spacings corresponding to distinct planes in BiSe and $NbSe_2$ (Fig. 2l). The crystal structure of FL-$(BiSe)_{1.10}NbSe_2$ is composed of alternating stacking of BiSe and $NbSe_2$ (Fig. 2m). Furthermore, elemental mapping (Fig. 2n) confirms the uniform distribution of bismuth, niobium, and selenium across the nanolayers, indicating the structural integrity of the misfitted phase post-exfoliation. The elemental percentage of $(BiSe)_{1.10}NbSe_2$ was performed by the inductively coupled plasma-optical emission spectroscopy (ICP-OES). Table S1 shows that the weight percentages of Bi:Nb:Se elements are 32.18 %: 16.34 %: 38.47 %, that the ratio of Bi:Nb:Se elements are approximately 1:1:3.

Fig. 3a displays the CV of FL-$(BiSe)_{1.10}NbSe_2$ over ten cycles between 0.01 and 3.0 V (vs. K^+/K) at a 0.1 mV s^{-1} scan rate. The CV allows clear observation of the conversion, alloying, and intercalation triple

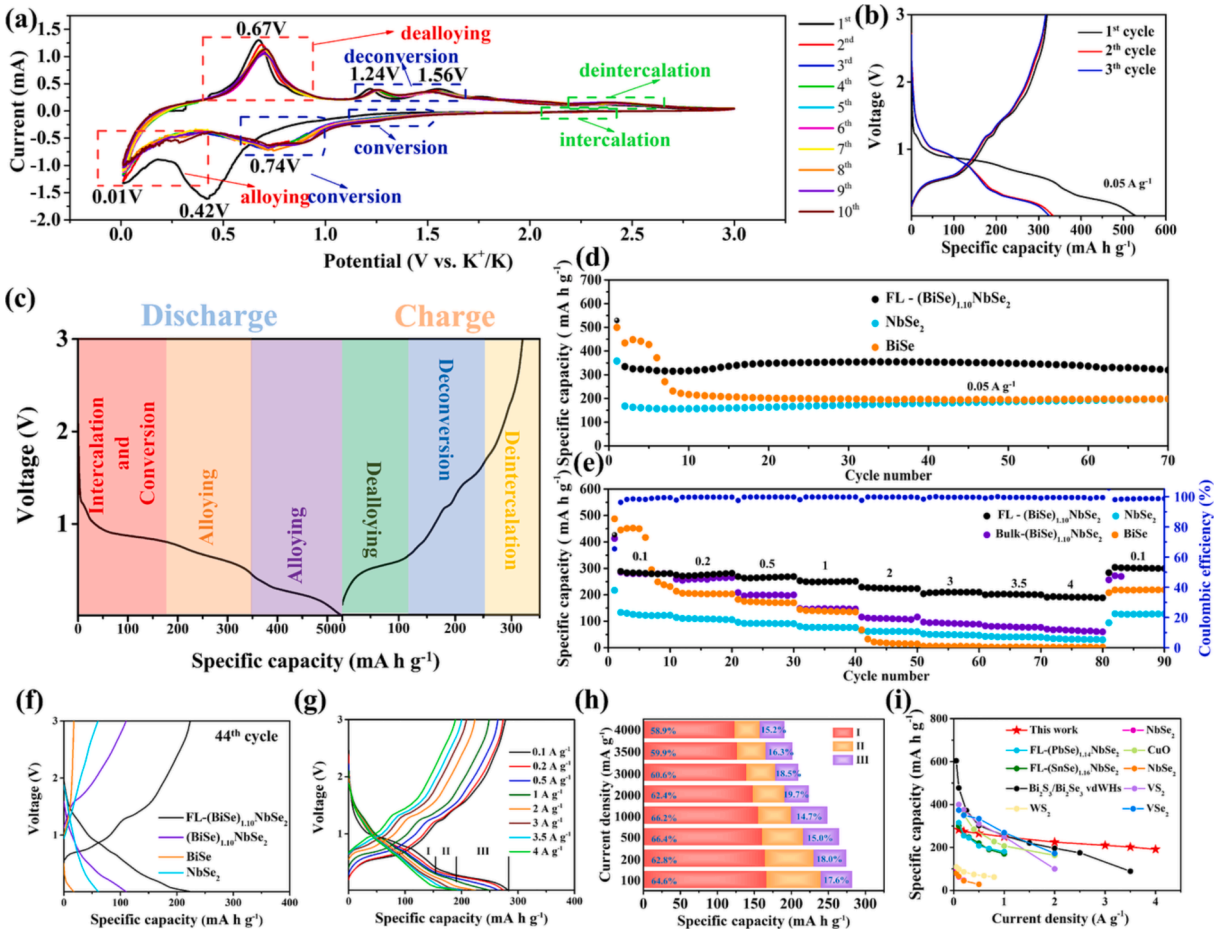

Fig. 3. Electrochemical performances and analysis of FL-$(BiSe)_{1.10}NbSe_2$, (a) CV curves at 0.1 mV s^{-1} of FL-$(BiSe)_{1.10}NbSe_2$. (b) GCD for first three cycles at 0.05 A/g. (c) GCD for 1st cycle at 0.05 A/g. (d) Cycling performance at a current density of 0.05 A/g. (e) Rate capability of FL-$(BiSe)_{1.10}NbSe_2$ and others in this work at various rates. (f) The corresponding GCD profiles for the 44th cycle at 2 A/g. (g) The corresponding GCD profiles at various rates. (h) Discharge capacity from the conversion plateau (I), the first alloying plateau (II), and the second alloying plateau (III) at different current rates. (i) A comparison between the results of this study and those reported in the literature.

mechanisms within FL-$(BiSe)_{1.10}NbSe_2$. The cathode peak at 0.42 V on the first scan, indicating the formation of a solid electrolyte interface (SEI). After the negative scan of the second cycle, the reduction peaks appear at 2.2 V, 1.3 V and 0.74 V, corresponding with the intercalation and conversion peak of $NbSe_2$, and the conversion reaction of BiSe. Another peak at 0.01 V represents the K_3Bi alloying reaction from K and Bi in BiSe. During the forward scan from 0 V to 3 V, BiSe undergoes a dealloying reaction at 0.67 V. Oxidation peaks at 1.24 V and 1.56 V relate to the deconversion of BiSe and $NbSe_2$, respectively [44]. Additionally, there are two subtle reduction peak between 1 V and 1.5 V and oxidation peaks between 2 V and 3 V corresponding to the intercalation reaction of $NbSe_2$ [45,46].

The CV of the FL-$(BiSe)_{1.10}NbSe_2$ anode in the first ten cycles exhibits curves similar to those obtained by superimposing the individual curves of BiSe and $NbSe_2$ (Fig. S8). Notably, the peaks for the conversion and deconversion reactions progressively vanish in the pure BiSe CV curve shown in Fig. S8a as the number of cycles increases. FL-$(BiSe)_{1.10}NbSe_2$, which doesn't show the same issues due to protection by the intercalation reaction product. This allows BiSe to fully undergo conversion and reconversion reactions, consistent with the enhanced capacity of FL-$(BiSe)_{1.10}NbSe_2$ compared to pure BiSe. The electrochemical performance of FL-$(BiSe)_{1.10}$ $NbSe_2$ was assessed using coin-type half cells. Fig. 3b displays the galvanostatic charge and discharge (GCD) curves for the first three cycles at 50 mA g^{-1}. The initial capacities for FL-$(BiSe)_{1.10}NbSe_2$ are 529.3 and 319.8 mA h g^{-1} for charge and discharge, respectively. The initial Coulomb efficiency is around 60.42 %, attributed to higher electrolyte consumption and a thicker SEI layer formation. Fig. 3c displays the reactions corresponding to each reaction platform in the GCD curve. Before comparing the performance of BiSe, $NbSe_2$, and FL-$(BiSe)_{1.10}NbSe_2$, the cycling performance of FL-(BiSe) $NbSe_2$ after the different sonication time was test (Fig. S9). The result shows that the capacity after 4 h sonication is higher than that before 4 h, indicating that it can be obtained the high level of layer-by-layer exfoliation material after 4 h. Fig. 3d shows the cycling performance of BiSe, $NbSe_2$, and FL-$(BiSe)_{1.10}NbSe_2$ at 0.05 A g^{-1}. Initially, BiSe's capacity drops from 450 mA h g^{-1} to about 200 mA h g^{-1} due to its fragile structure, compromising its capacity. In contrast, $NbSe_2$ has a robust structure and good conductivity, allowing it to sustain capacity close to 200 mA h g^{-1}, with a gradual increase. FL-$(BiSe)_{1.10}NbSe_2$ exhibits a reversible capacity of around 350 mA h g^{-1}, merging BiSe's high capacity with $NbSe_2$'s cycle stability, indicative of the efficient K^+ insertion/deintercalation process. The unique interlayer structure inherent in FL-$(BiSe)_{1.10}NbSe_2$ provides a robust and highly conductive scaffold for the fragile and poorly conductive BiSe, so it exhibits better cycling performance. However, the poor electrical conductivity affects long-term cycle stability. Therefore, through mixing FL-(BiSe)$NbSe_2$ with graphite (FL-(BiSe)$NbSe_2$@G), the cycling performance can be improved (Fig. S10). The rate capability of various materials was conducted from 0.1 to 4 A g^{-1} to understand the effect of the misfit layered structure on PIB, as seen in Fig. 3e. For FL-$(BiSe)_{1.10}NbSe_2$, as current density increases from 0.1 to 4 A g^{-1}, the reversible capacities are 283, 275, 265, 249, 224, 210, 202, and 191 mA h g^{-1}. Notably, when the

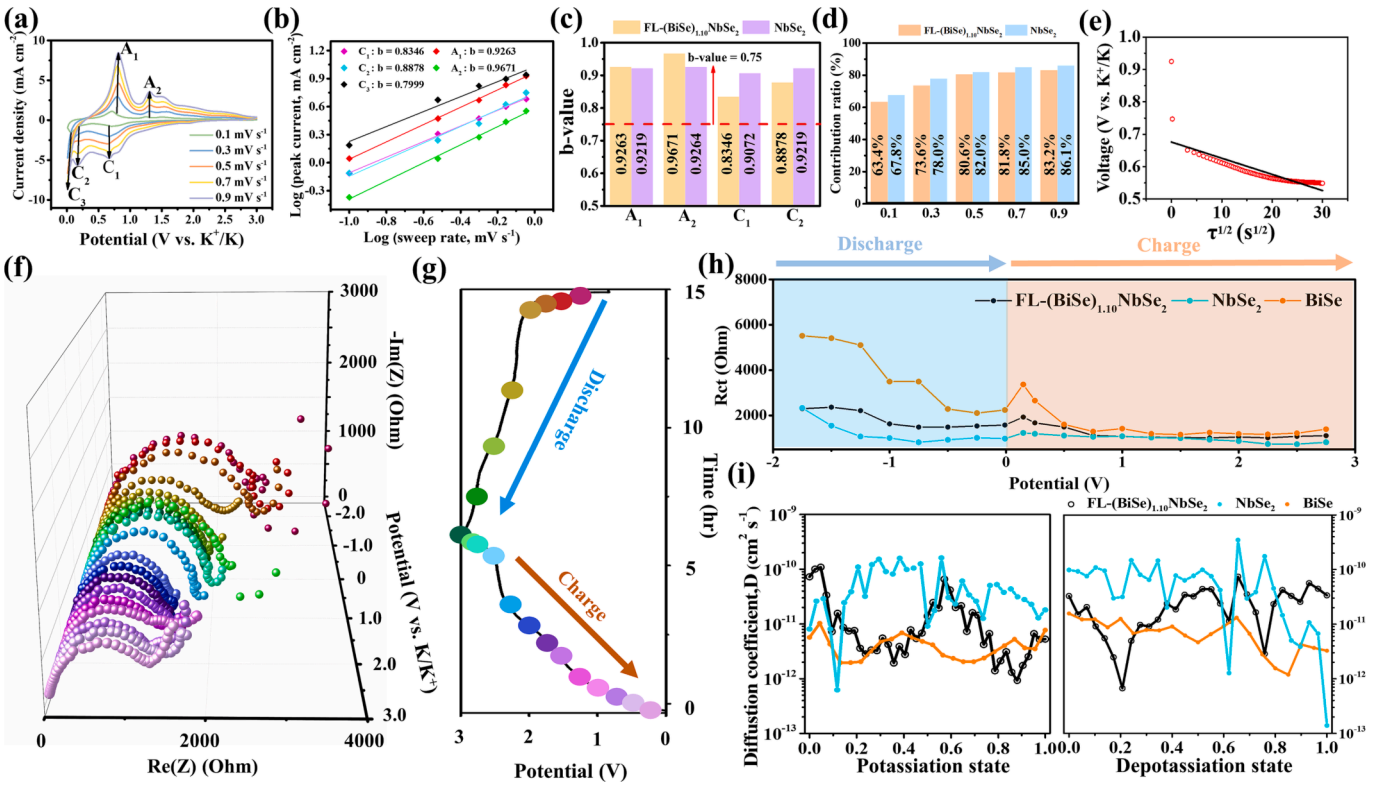

Fig. 4. (a) CV curves of FL-(BiSe)$_{1.10}$NbSe$_2$ from 0.1 mV s^{-1} to 0.9 mV s^{-1}, (b) b values in linear regression are associated with the plotted data in graph (a), (c) Calculated b values for FL-(BiSe)$_{1.10}$NbSe$_2$ and NbSe$_2$ at anode and cathode, (d) Capacitive-controlled contribution at different scan rates, (e) voltage variation against $\tau^{1/2}$, (f) In-situ EIS curves, (g) corresponding voltage profile and (h) calculated impedances, (i) corresponding D_{k+} of each material.

current density reverts to 0.1 A g^{-1}, the capacity recovers to 301 mA h g^{-1}. (BiSe)$_{1.10}$NbSe$_2$, while stable at high rates compared to FL-(BiSe)$_{1.10}$NbSe$_2$, exhibits a lower reversible capacity. The robustness and conductivity of NbSe$_2$, combined with its support for internal BiSe, yield a synergistic effect enhancing potassium storage, despite BiSe's limited capacity at high rates. Consequently, (BiSe)$_{1.10}$NbSe$_2$ displays strong rate capability and reversibility at high rates. Fig. 3f depicts the GCD curves of different materials after 44 cycles. FL-(BiSe)$_{1.10}$NbSe$_2$ and (BiSe)$_{1.10}$NbSe$_2$ exhibit similar reaction trends but differ in capacitance values at high rates, indicating no side reactions from ultrasonic vibration during FL-(BiSe)$_{1.10}$NbSe$_2$ preparation. In contrast, BiSe offers limited capacity at high rates because of its fragility and reduced conductivity. In Fig. 3g, the GCD curves of the rate performance of FL-(BiSe)$_{1.10}$NbSe$_2$ clearly reveal three distinct plateaus. The first plateau (I) corresponds to the conversion reaction of K_2Se (theoretical capacity: 678 mA h g^{-1}), the second plateau (II) corresponds to the alloying reaction forming KBi_2 (theoretical capacity: 64 mA h g^{-1}), and the third plateau (III) corresponds to the alloying reaction of KBi_2 alloying into K_3Bi (theoretical capacity: 322 mA h g^{-1}). As shown in Fig. 3h, BiSe within FL-(BiSe)$_{1.10}$NbSe$_2$ can undergo a complete reduction reaction with the assistance of the NbSe$_2$ conductive framework, allowing plateau I to deliver 58.9 % of its discharge capacity at a high current density of 4 A g^{-1}, not far from the 64.6 % observed at 0.1 A g^{-1}. These results confirm that the fragility and low conductivity of the BiSe structure in FL-(BiSe)$_{1.10}$NbSe$_2$ can be overcome by incorporating the NbSe$_2$ framework, enhancing the overall electrical conductivity, and fully exploiting the electrochemical performance of BiSe's high capacity [40]. Additionally, the cycling performance of FL-(BiSe)$_{1.10}$NbSe$_2$ at current densities ranging from 100 mA g^{-1} to 500 mA g^{-1} were investigated. Fig. S11 shows FL-(BiSe)$_{1.10}$NbSe$_2$ can deliver the capacity of 340 mA h g^{-1} at 100 mA g^{-1} after 80 cycles. Even at 500 mA g^{-1}, it can maintain a capacity of 275 mA h g^{-1}. The rate capability of FL-(BiSe)$_{1.10}$NbSe$_2$ negative electrode material was compared with other relevant carbon-free materials in PIBs, as shown in Fig. 3i. For non-carbon-based anode materials, the electrochemical stability is effectively enhanced by employing laminar and layered structures, and the construction of heterogeneous structures significantly improves their electrochemical performance. The FL-(BiSe)$_{1.10}$NbSe$_2$, achieved by combining layered NbSe$_2$ with BiSe, forms a heterogeneous structure with a conversion-alloying-intercalation triple mechanism, enhancing its intrinsic electrochemical rate capability. It can be observed in Fig. 3i [8,25,40,47–52], except for FL-(BiSe)$_{1.10}$NbSe$_2$ and Bi_2S_3/Bi_2Se_3 vdWHs, the rate capability of most materials is limited to around 2 A g^{-1} or below. Although the capacity at low rates is superior to FL-(BiSe)$_{1.10}$NbSe$_2$ for some materials, at high current density (4 A g^{-1}), FL-(BiSe)$_{1.10}$NbSe$_2$ evidently demonstrates the most outstanding performance among carbon-free materials, showing excellent rate capability.

FL-(BiSe)$_{1.10}$NbSe$_2$ outperforms other materials in cycling and K$^+$ storage due to its pseudocapacitance and diffusion behavior. CV tests on FL-(BiSe)$_{1.10}$NbSe$_2$ and NbSe$_2$ electrodes at varying scan rates (0.1 to 0.9 mV s^{-1}) showed similar curve shapes (Fig. 4a, S12, and S13). Increasing scan rates led to shifts in cathode and anode peaks due to ohmic resistance. The current is influenced by surface-controlled and diffusion-controlled reactions, as described by a specific equation:

$$i = av^b (0.5 \le b \le 1) \quad (1)$$

$$logi = blogv + \log a \quad (2)$$

Equation (1) relates peak current (i) to scan rate (v) through adjustable constants a and b in a power law. The value of b is crucial for the kinetic role of the electrode surface. A b value of 0.5 or 1.0 signifies whether the material's electrochemical process is diffusion-controlled or capacitance-controlled, respectively. Fig. 4b, c, and S13b show that the calculated b values for peaks in FL-(BiSe)$_{1.10}$NbSe$_2$ and NbSe$_2$ exceed 0.75. Values nearing 1.0 indicate a pseudocapacitive charge storage mechanism, pointing out NbSe$_2$'s stable structure and superior

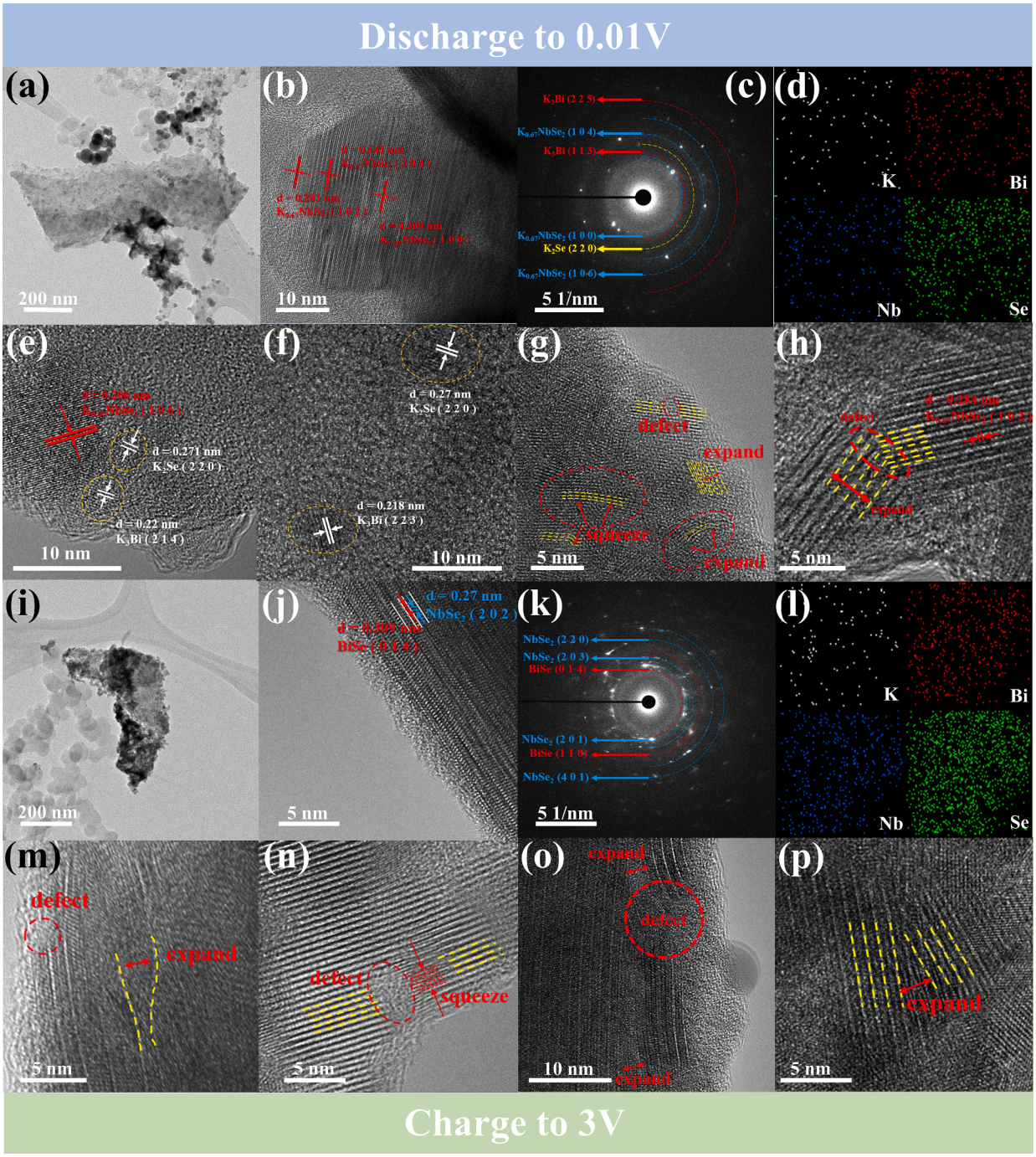

Fig. 5. Low magnification TEM images, HRTEM images, SAED patterns and EDS elements mapping of the cycled FL-$(BiSe)_{1.10}NbSe_2$: (a–h) discharged to 0.01 V, (i–p) charged to 3 V.

conductivity for high-rate capability. A constant k allows for quantitative analysis of the capacitance-controlled process.

$$i = k_1 v + k_2 v^{0.5} \quad (3)$$

k_1v and $k_2v^{0.5}$ correspond to non-Faradaic and Faradaic reactions, respectively. At a scan rate of 0.9 mV s^{-1} in Fig. S12, the capacitive contribution comprises 83.16 % of the CV curve's total area, indicating that capacitance-controlled current prevails over diffusion-controlled current, boosting high-rate performance. Figs. S12 and S13 illustrate an amplified surface capacitance effect in FL-$(BiSe)_{1.10}NbSe_2$ and $NbSe_2$ at elevated scan rates, leading to its prominent high-rate K^+ storage and swift charge/discharge traits. Fig. 4d indicates that $NbSe_2$ consistently surpasses FL-$(BiSe)_{1.10}NbSe_2$ in capacitance contribution across all scan rates, stemming from BiSe's fragility and poor conductivity [45].

The stability and superior conductivity of $NbSe_2$ enhance BiSe's rate performance, with the enhanced characteristics of FL-$(BiSe)_{1.10}NbSe_2$ resulting from the synergistic interplay of $NbSe_2$ and BiSe. In-situ EIS analysis (Fig. 4f-h, S14, and S15) reveals varying Rct values during the first charge and discharge cycle. $NbSe_2$'s superior conductivity results in a lower Rct compared to FL-$(BiSe)_{1.10}NbSe_2$ and BiSe. Supported by $NbSe_2$'s conductive framework, FL-$(BiSe)_{1.10}NbSe_2$ exhibits an Rct between the two. The layered structure synergizes $NbSe_2$'s stability and BiSe's reactivity, enhancing K^+ storage. To study the diffusion kinetics of FL-$(BiSe)_{1.10}NbSe_2$, $NbSe_2$, and BiSe electrodes, GITT was used to

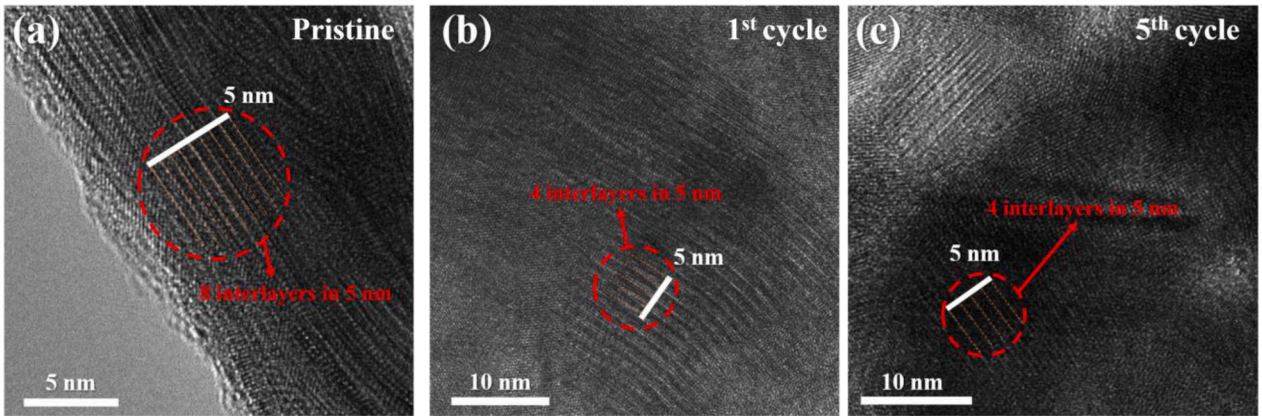

Fig. 6. HRTEM images depict changes in lattice spacing for FL-$(BiSe)_{1.10}NbSe_2$ under the following conditions: (a) pristine, (b) after the 1st cycle, and (c) after the 5th cycle.

measure the diffusion coefficient of K^+ (D_{K+}) in Figs. 4, S16 and S17 [53]. The corresponding polarizer thickness is shown in Fig. S18. For the linear relationship between E_τ and $\tau^{1/2}$ shown in Fig. 4e [54]. As shown in Fig. 4i, $NbSe_2$ electrode exhibited a higher average D_{K+} compared to FL-$(BiSe)_{1.10}NbSe_2$ and BiSe electrodes. However, in the potassium-intercalated state, the diffusion rate of $NbSe_2$ fluctuated significantly in the range of 10^{-9} to 10^{-13} cm^2 s^{-1}, whereas FL-$(BiSe)_{1.10}NbSe_2$ displayed a stable D_{K+} trend, falling in between the values of $NbSe_2$ and BiSe, demonstrating a stable diffusion rate within the range of 10^{-10} to 10^{-11} cm^2 s^{-1}. These correspond with the trend observed in the change of Rct values in the in-situ EIS analysis, indicating that throughout the electrochemical performance, FL-$(BiSe)_{1.10}NbSe_2$ maintains Rct values between those of $NbSe_2$ and BiSe. GITT measurements confirm that the FL-$(BiSe)_{1.10}NbSe_2$ electrode has achieved enhanced reaction kinetics, effectively improving the high-rate cycling capability of potassium ions through the synergistic effect between $NbSe_2$ and BiSe [33].

During cyclic testing, we employed ex-situ TEM and HRTEM to study the lattice structure and phase evolution of the FL-$(BiSe)_{1.10}NbSe_2$ anode (Fig. 5). Fig. 5a and 5i reveal stable morphology at both 0.01 V and 3 V states. Additional ex-situ HRTEM and SAED studies confirmed this stability across various charge and discharge states. At 0.01 V, SAED patterns revealed products from conversion, alloying, and intercalation reactions (Fig. 5c). Specifically, K_3Bi alloy showed (225) and (113) planes, K_2Se had a (220) plane, and $K_{0.67}NbSe_2$ displayed (100), (104), and (106) planes. Fig. 5b and 5e-h from HRTEM analyses display multiple lattice spacings. The spacings of 0.141 nm, 0.283 nm, 0.309 nm, and 0.206 nm in Fig. 5b and 5e are associated with the (204), (102), (100), and (106) planes of $K_{0.67}NbSe_2$, respectively. Fig. 5e and 5f show lattice spacings of 0.218 nm and 0.220 nm corresponding to the (223) and (214) planes of K_3Bi, while 0.27 nm and 0.271 nm relate to the (220) plane of K_2Se. The EDS mapping (Fig. 5d) shows a uniform element distribution. Upon recharging to 3.0 V, Fig. 5i-p display lattice details for reversible phases BiSe and $NbSe_2$. Specifically, in Fig. 5k, SAED rings correspond to the (014) and (110) planes of BiSe and the (220), (203), (201), and (401) planes of $NbSe_2$. Fig. 5j depicts lattice spacings of 0.27 nm and 0.309 nm, corresponding to the (202) plane of $NbSe_2$ and the (014) plane of BiSe, respectively. Matching the findings in Fig. 1h confirms the preservation of FL-$(BiSe)_{1.10}NbSe_2$'s misfit phase structure after cycling. The uniform element distribution in the EDS diagram occurs after one cycle (Fig. 5l). Lattice distortion in the large-scale heterostructure weakens diffraction peaks in the misfit layered structure. To clarify FL-$(BiSe)_{1.10}NbSe_2$'s reaction mechanism, ex-situ XRD was performed. As show in Fig. S19, in addition to the peak of Cu and parafilm, these broad peaks appear from 25° to 35° when discharging to 0.01 V. The broad peak makes analysis difficult. Fortunately, when charging to 3 V, the peaks of FL-$(BiSe)_{1.10}NbSe_2$ were observed, indicating the reversible reaction. On the other hand, the peaks of FL-$(BiSe)_{1.10}NbSe_2$ can correspond to the peaks of pure BiSe and pure $NbSe_2$, respectively (Fig. 3a and S8). Therefore, it can be speculated that BiSe and $NbSe_2$ react with K^+, respectively. In order to figure out the phase transition of FL-$(BiSe)_{1.10}NbSe_2$, ex-situ XRD was performed on $NbSe_2$ (Fig. S20). The XRD peak at 14.8° shifts to a lower angle during discharge, forming $K_{0.67}NbSe_2$, and reverses during charging, confirming structural integrity. However, residual K^+ in $NbSe_2$ at 3 V shifts peaks to a lower angle, failing to return to their original positions, as corroborated by the EDS chart in Fig. 5l. During the charging and discharging process, we observe subtle peaks associated with Nb, K_2Se, K_5Se_3, and Se which implies that alongside intercalation, some $NbSe_2$ undergoes deconversion, ultimately returning to its $NbSe_2$ phase by the end of the cycle. Using HRTEM, we studied the lattice structure and elemental changes caused by potassium intercalation. K^+ insertion during discharge expands the chalcogenide layers unevenly, resulting in squeezing deformations and subsequent lattice distortions and defects, as evident in Fig. 5g and 5 h. During the extraction of K^+ in phase charging, the lattice contracts, bringing the bands closer, as evidenced in Fig. 5n. Despite this contraction, remnants of dislocations and vacancies from the potassium insertion process remain visible, especially in Fig. 5m–p. These defects, far from being mere artifacts, play a pivotal role in future cycles by offering enhanced pathways for K^+ diffusion, improving the electrochemical reaction kinetics [25].

Using HRTEM, as depicted in Fig. 6a–c, we observed changes in lattice spacing across cycles. The findings indicate a notable expansion in the lattice following K^+ insertion/deintercalation relative to its original configuration. Yet, the spacing after the first and fifth cycles remains remarkably consistent, with no discernible degradation of the core lattice patterns. This uniformity emphasizes the robustness of the $NbSe_2$ structure, effectively withstanding the structural challenges introduced by the K^+. The distinctive misfit layered design efficiently disperses mechanical stresses, stabilizing interlayer distances. Consequently, the core metal chalcogenide, BiSe, retains its reactivity across cycles, protected from rapid disintegration usually caused by significant volumetric changes during cycling.

We developed two models to study stress distribution using FEA. The first model features nanocrystalline materials with a BiSe core and six BiSe faces (Fig. 7a-c), while the second has a BiSe core with $NbSe_2$ layers on the top and bottom (Fig. 7d-f). We simulated the potassium intercalation process using thermal expansion, with volume changes noted in Table S2. Constants for the simulations, including Young's modulus, Poisson's ratio (Table S3), and thermal expansion coefficient, are provided. Compared to $NbSe_2$, BiSe's properties—its greater thermal expansion coefficient and lower Young's modulus—cause more stress and deformation during the potassium intercalation process. Undissipated stress leads to interface breakdown when BiSe crystals are closely packed, prompting K^+ to form a new SEI layer. However, the

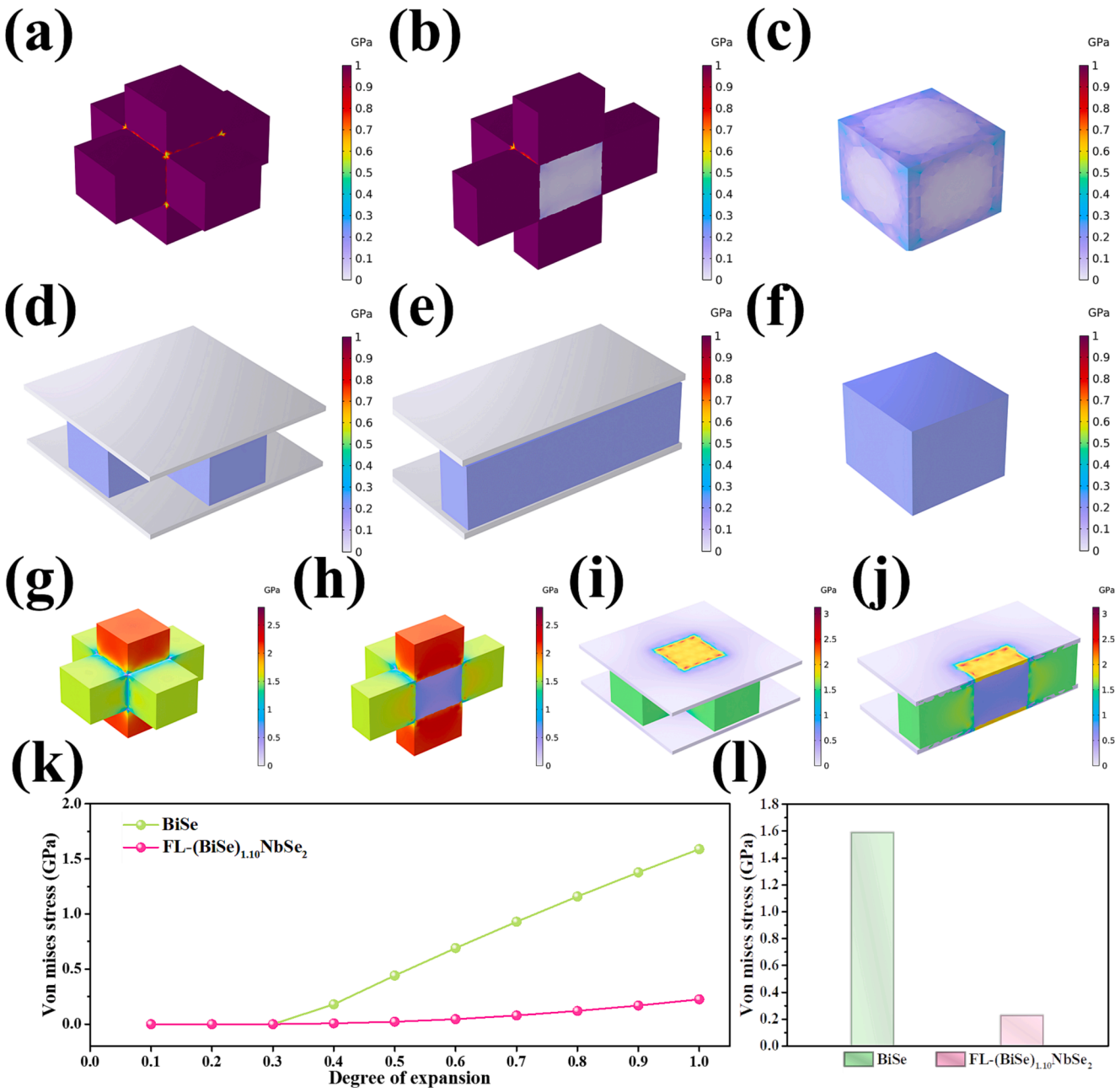

Fig. 7. Finite element analysis. The stress distribution model for (a-c) BiSe nanocrystals and (d-f) $(BiSe)_{1.10}NbSe_2$. Linear distributions of externally applied vertical Von-Mise stress on (g, h) BiSe and (i, j) $(BiSe)_{1.10}NbSe_2$ structural units. (k) The corresponding stress values at various degrees of expansion, and (l) the value after complete expansion.

formation of the SEI layer diminishes the active material, shortening the battery's lifespan. Pure BiSe materials show a high initial capacity that drops in subsequent cycles, as behavioral evidenced in Fig. 2b and 2d. By integrating $NbSe_2$, known for its high Young's modulus, into a misfitted bilayer setup, we successfully controlled BiSe's expansion and optimized stress distribution between the two materials. Consequently, the combined $(BiSe)_{1.10}NbSe_2$ MLC showed enhanced structural and electrochemical resilience relative to unjoined BiSe. In Fig. 7k, when the expansion factor of BiSe nanocrystals is approximately 0.3, the slope sharply increases, indicating that the nanocrystals cannot withstand the stress and therefore fracture. Subsequently, the addition of $NbSe_2$ effectively reduces the stress, preventing the internal BiSe nanocrystals from fracturing due to excessive stress. Fig. 7l displays the maximum stress values for each model when the expansion factor is 1.0 [55]. The material's external stress resistance was tested using vertical Von-Mises stress (Fig. 7g-j) [56]. The $(BiSe)_{1.10}NbSe_2$ bilayer displayed less central stress than pure BiSe due to the effective stress distribution of the $NbSe_2$ outer layer. The material can better handle external stresses by utilizing $NbSe_2$'s superior mechanical properties to envelop BiSe in this misfitted bilayer. Moreover, the protective $NbSe_2$ layer helps offset stresses from volume changes in BiSe during potassium cycling, enhancing its electrochemical performance.

Fig. 8 illustrates the visual differences and conditions before and after electrochemical cycling tests for FL-$(BiSe)_{1.10}NbSe_2$, $(BiSe)_{1.10}NbSe_2$, BiSe, and $NbSe_2$ materials. BiSe experiences significant material expansion and structural damage due to the conversion-alloying reaction, resulting in material deformation and a substantial decrease in capacity after cycling. After cycling, $NbSe_2$'s structure remains stable with only a slight interlayer expansion because it has sufficient interlayer spacing to accommodate the volume expansion of the

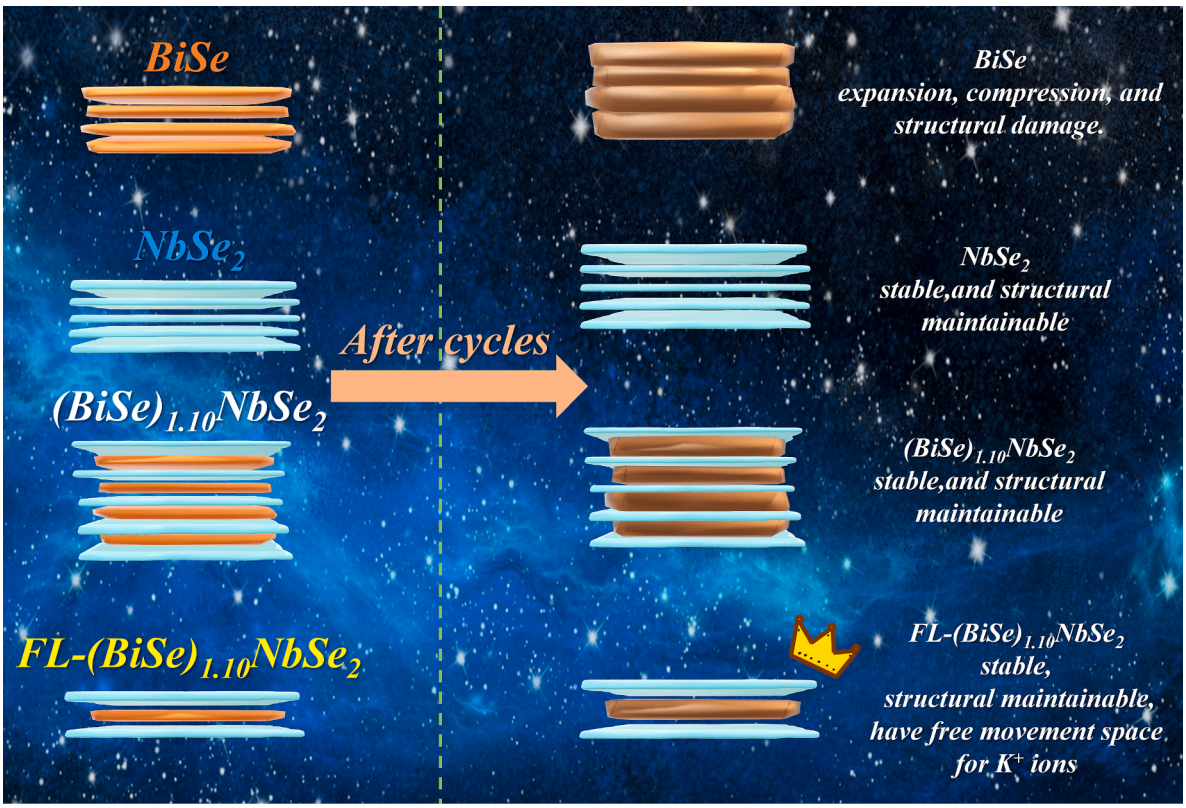

Fig. 8. Schematic diagram of structural changes after the reaction processes. The $NbSe_2$ framework effectively protects BiSe and mitigates structural damage.

material. $(BiSe)_{1.10}NbSe_2$, by safeguarding BiSe after the conversion-alloying reaction within the framework of $NbSe_2$, effectively maintains overall structural stability. However, the multilayer structure restricts the free movement space for K^+, reducing its capacitance. FL-$(BiSe)_{1.10}NbSe_2$ addresses the shortcomings of $(BiSe)_{1.10}NbSe_2$ by providing sufficient free mobility space for K^+, enhancing stability and capacity, and fully capitalizing on the advantages of the conversion, alloying, and intercalation triple mechanisms.

Utilizing the distinct phase structure of FL-$(BiSe)_{1.10}NbSe_2$, featuring alternating molecular layers, we aimed to counteract the limitations inherent to BiSe and $NbSe_2$. This enhanced composite is suitable for inclusion in a PIHC system with various cathode materials. Specifically, we employed the advantageous reaction kinetics and potassium storage capacity of FL-$(BiSe)_{1.10}NbSe_2$ to construct an asymmetric PIHC comprising a FL-$(BiSe)_{1.10}NbSe_2$ anode and a commercial activated carbon (AC) cathode (Fig. 9a). This asymmetric configuration was employed to elucidate the merits of the misfit phase structure in facilitating electron and K^+ transport. Owing to the accelerated diffusion kinetics and superior electrochemical performance of K^+ in FL-$(BiSe)_{1.10}NbSe_2$, FSI ions in the electrolyte undergo non-faradaic adsorption and desorption processes on the activated carbon cathode, enhancing the energy density. Prior to the PIHC assembly, the FL-$(BiSe)_{1.10}NbSe_2$ anode was pre-activated for 20 cycles to minimize irreversible capacity loss during the initial cycles and ensure thorough K^+ intercalation into the material. To relieve electrolyte decomposition at elevated operating voltages, we confined the operating voltage window to 0.5–3.8 V. An optimal mass ratio of 1:1.2 for FL-$(BiSe)_{1.10}NbSe_2$ to AC was determined to maximize power output. Subsequent electrochemical characterization of the FL-$(BiSe)_{1.10}NbSe_2$//AC system included a representative CV curve (Fig. 9b). Additionally, Fig. 9c illustrates the charge and discharge profiles of FL-$(BiSe)_{1.10}NbSe_2$//potassium half-cell, AC//potassium half-cell, and the FL-$(BiSe)_{1.10}NbSe_2$//AC PIHC at a current density of 50 mA g^{-1}. The nearly linear, non-isosceles triangular charge/discharge curve indicates a synergistic pseudocapacitive contribution to charge storage [57]. Rate performance was evaluated at varying current densities (Fig. 9d and 9e), with energy densities ranging from 81 to 32 Wh kg^{-1} based on the combined weight of FL-$(BiSe)_{1.10}NbSe_2$ and activated carbon. Notably, the system displayed admirable reversibility, maintaining an energy density of 61 Wh kg^{-1} upon returning to a current density of 1 A g^{-1}. The Ragone plot (Fig. 9f) revealed a maximum power density of 5823.6 W kg^{-1} at an energy density of 32.4 Wh kg^{-1}. Moreover, long-term cycling tests (Fig. 9g) exhibited an energy density of 42 Wh kg^{-1} of the initial capacity after 2000 cycles at a high current density of 1000 mA g^{-1}, demonstrating the system's robustness and longevity.

4. Conclusion

This work underscores the significance of systematically designing misfitted layered structures. Utilizing the intercalation reaction product as a framework during the reaction process, significantly alleviates the internal stress generated within FL-$(BiSe)_{1.10}NbSe_2$ during the conversion, alloying, and intercalation triple mechanisms, as BiSe expands during the conversion-alloying. FEA simulations predicted that this structure exhibits optimal stress-dispersion functionality, consistent with the results. Subsequently, employing point probe ultrasonication to selectively delaminate the $NbSe_2$ vdW gaps, we obtained FL-$(BiSe)_{1.10}NbSe_2$, demonstrating excellent electrochemical performance. Given the limited literature on the application of MLC materials in potassium-ion storage systems, our work successfully unveils the electrochemical performance of MLC materials and their practical applications through a series of electrochemical tests. Finally, by applying FL-$(BiSe)_{1.10}NbSe_2$ in PIHCs, we validate the stable performance of carbon-free MLC materials in potassium-ion storage systems. This study is the first to apply MLC materials in capacitors, offering a new method for developing potassium-ion intercalation anodes. Our results highlight a promising direction for MLC materials in novel applications.

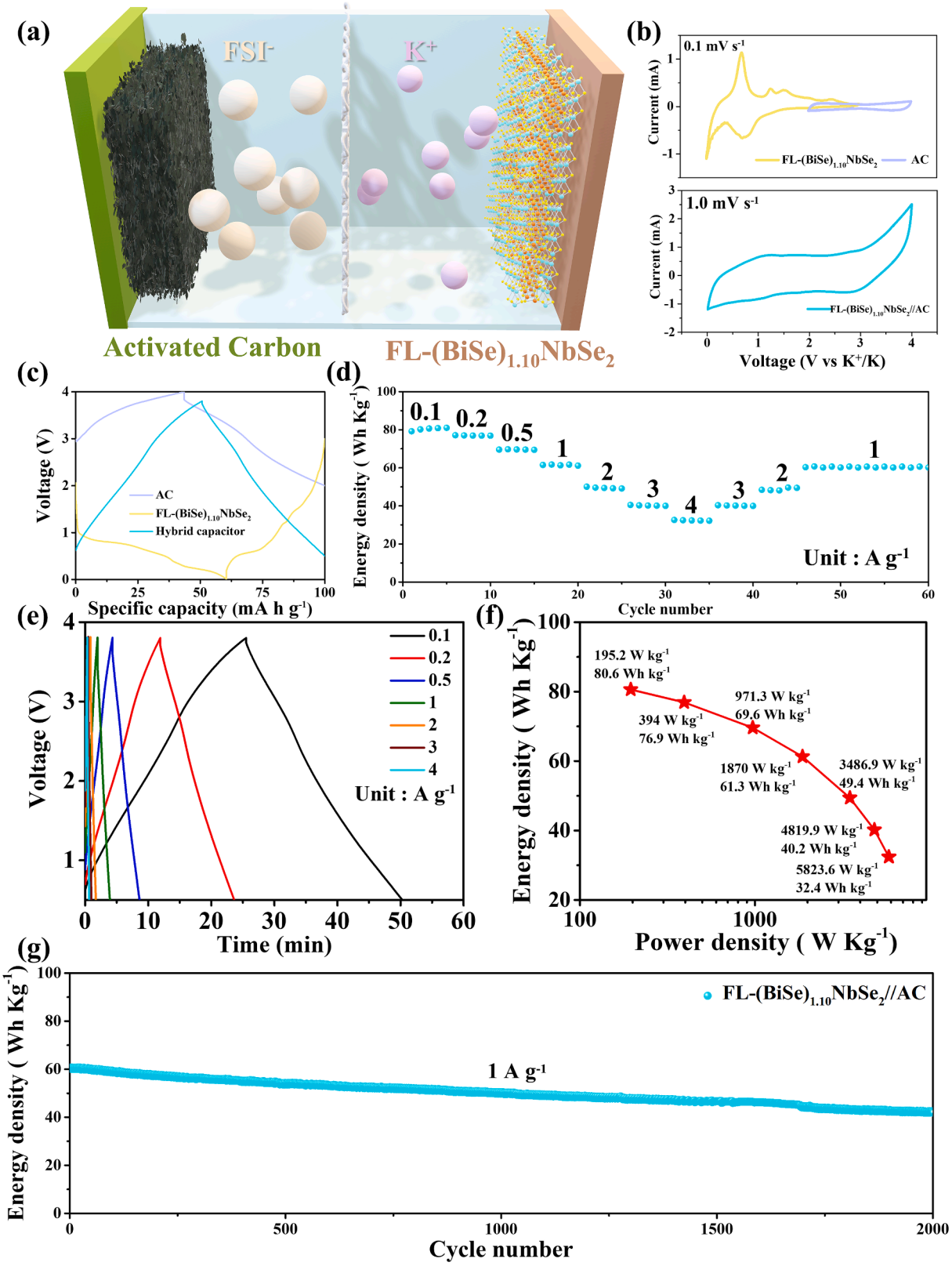

Fig. 9. (a) Schematic diagram of a FL-$(BiSe)_{1.10}NbSe_2$//AC hybrid capacitor. (b) CV curves of the AC half-cell, the FL-$(BiSe)_{1.10}NbSe_2$ half-cell and the FL-$(BiSe)_{1.10}NbSe_2$//AC PIHCs. (c) Normalized GCD curves of the AC half-cell, FL-$(BiSe)_{1.10}NbSe_2$ half-cell and the FL-$(BiSe)_{1.10}NbSe_2$//AC PIHCs. (d) Rate capability performance. (e) Normalized GCD curves plotted correspond to rate capability of the FL-$(BiSe)_{1.10}NbSe_2$//AC PIHCs. (f) Ragone plot of the FL-$(BiSe)_{1.10}NbSe_2$//AC PIHCs. (g) Long-term cycling performance of the FL-$(BiSe)_{1.10}NbSe_2$//AC PIHCs at 1.0 A/g.

CRediT authorship contribution statement

Shou-Shan Mai: Data curation, Formal analysis. **Yi-Chun Yang:** Data curation, Writing – review & editing. **Hsing-Yu Tuan:** Conceptualization, Investigation, Resources, Writing – original draft.

Declaration of competing interest

The authors declare that they have no known competing financial interests or personal relationships that could have appeared to influence the work reported in this paper.

Data availability

Data will be made available on request.

Acknowledgments

This work was financially supported by the 2030 Cross-Generation Young Scholars Program provided by the National Science and Technology Council of Taiwan (NSTC 112-2628-E-007-010). H.-Y. Tuan acknowledges additional financial support from National Tsing Hua University, Taiwan, through Grant No. 109QI030E1. The authors would like to express their gratitude for the technical assistance provided by Mr. Yung-Sheng Chen at the Instrumentation Center of National Tsing Hua University.

Appendix A. Supplementary data

Supplementary data to this article can be found online at https://doi.org/10.1016/j.cej.2024.149289.

References

[1] X. Min, J. Xiao, M. Fang, W.A. Wang, Y. Zhao, Y. Liu, A.M. Abdelkader, K. Xi, R. V. Kumar, Z. Huang, Potassium-ion batteries: outlook on present and future technologies, Energ Environ. Sci. 14 (4) (2021) 2186–2243.
[2] W. Zhang, Y. Liu, Z. Guo, Approaching high-performance potassium-ion batteries via advanced design strategies and engineering, Sci. Adv. 5 (5) (2019) eaav7412.
[3] J. Zheng, Y. Sun, Y. Wu, J. Rong, Z. Wang, H. Li, L. Niu, Ultralong cycle life and high rate potassium ion batteries enabled by multi-level porous carbon, J. Power Sources 492 (2021) 229614.
[4] X. Wu, Y. Chen, Z. Xing, C.W.K. Lam, S.S. Pang, W. Zhang, Z. Ju, Advanced carbon-based anodes for potassium-ion batteries, Adv. Energy Mater. 9 (21) (2019) 1900343.
[5] K.-C. Lin, M.-W. Lin, M.-N. Hsu, G. Yu-Chen, Y.-C. Chao, H.-Y. Tuan, C.-S. Chiang, Y.-C. Hu, Graphene oxide sensitizes cancer cells to chemotherapeutics by inducing early autophagy events, promoting nuclear trafficking and necrosis, Theranostics 8 (9) (2018) 2477.
[6] Z. Liu, J. Wang, B. Lu, Plum pudding model inspired $KVPO_4F$@xu/63DC as high-voltage and hyperstable cathode for potassium ion batteries, Sci. Bull. 65 (15) (2020) 1242–1251.
[7] J. Yang, Z. Ju, Y. Jiang, Z. Xing, B. Xi, J. Feng, S. Xiong, Enhanced capacity and rate capability of nitrogen/oxygen dual-doped hard carbon in capacitive potassium-ion storage, Adv. Mater. 30 (4) (2018) 1700104.
[8] Y. Huang, R. Haider, S. Xu, K. Liu, Z.-F. Ma, X. Yuan, Recent progress of novel non-carbon anode materials for potassium-ion battery, Energy Storage Mater. 51 (2022) 327–360.
[9] P.-W. Chien, C.-B. Chang, H.-Y. Tuan, High-entropy two-dimensional metal phosphorus trichalcogenides boost high-performance potassium ion storage devices via electrochemical reconstruction, Energy Storage Mater. 61 (2023) 102853.
[10] Y. Zhu, L. Peng, Z. Fang, C. Yan, X. Zhang, G. Yu, Structural engineering of 2D nanomaterials for energy storage and catalysis, Adv. Mater. 30 (15) (2018) 1706347.
[11] H.-J. Yang, C.-Y. Chen, F.-W. Yuan, H.-Y. Tuan, Designed synthesis of solid and hollow Cu2–x Te nanocrystals with tunable near-infrared localized surface plasmon resonance, J. Phys. Chem. C 117 (42) (2013) 21955–21964.
[12] H.G. Oh, S.H. Yang, Y.C. Kang, S.-K. Park, N-doped carbon-coated $CoSe_2$ nanocrystals anchored on two-dimensional MXene nanosheets for efficient electrochemical sodium- and potassium-ion storage, Int. J. Energy Res. 45 (12) (2021) 17738–17748.
[13] Z. Xiao, J. Meng, F. Xia, J. Wu, F. Liu, X. Zhang, L. Xu, X. Lin, L. Mai, K+ modulated K+/vacancy disordered layered oxide for high-rate and high-capacity potassium-ion batteries, Energy Environ. Sci. 13 (9) (2020) 3129–3137.
[14] Y. Jin Jang, S.-K. Park, Rational design of hierarchical Ni-Mo bimetallic Selenide/N-doped carbon microspheres toward high–performance potassium ion batteries, Appl. Surf. Sci. 583 (2022) 152491.
[15] Y. Wu, Y. Sun, J. Zheng, J. Rong, H. Li, L. Niu, Exploring MXene-based materials for next-generation rechargeable batteries, J. Phys.: Energy 3 (3) (2021) 032009.
[16] H. Tan, Y. Feng, X. Rui, Y. Yu, S. Huang, Metal chalcogenides: paving the way for high-performance sodium/potassium-ion batteries, Small Methods 4 (1) (2020) 1900563.
[17] S. Palchoudhury, K. Ramasamy, J. Han, P. Chen, A. Gupta, Transition metal chalcogenides for next-generation energy storage, Nanoscale Adv. 5 (10) (2023) 2724–2742.
[18] S.-S. Mai, K.-Y. Hsiao, Y.-C. Yang, Y.-R. Lu, M.-Y. Lu, Y.-Y. Hsieh, C.-B. Chang, H.-Y. Tuan, Synchronous regulation of Schottky/pn dual junction in Prussian blue-derived Janus heterostructures: A path to ultrafast long life potassium ion batteries, Chem. Eng. J. 474 (2023) 145992.
[19] Y. Du, W. Weng, Z. Zhang, Y. He, J. Xu, J. Sun, J. Liao, J. Bao, X. Zhou, Candied-Haws-like architecture consisting of FeS_2@C core–shell particles for efficient potassium storage, ACS Mater. Lett. 3 (4) (2021) 356–363.
[20] H. Lee, H. McKinzie, D. Tannhauser, A. Wold, The low-temperature transport properties of NbSe2, J. Appl. Phys. 40 (2) (1969) 602–604.
[21] A. Shokri, A. Yazdani, B. Barakati, Comparison between layering $NbSe_2$ and rod characteristic of MgB2 by investigation of elastic constants, J. Phys.: Conf. Series, IOP Publishing (2018) 012026.
[22] Y. Subramanian, G.K. Veerasubramani, M.-S. Park, D.-W. Kim, Investigation of layer structured NbSe2 as an intercalation anode material for sodium-ion hybrid capacitors, J. Electrochem. Soc. 166 (4) (2019) A598.
[23] D.F. Carrasco, S. García-Dalí, S. Villar-Rodil, J.M. Munuera, E. Raymundo-Piñero, J.I. Paredes, $NbSe_2$ nanosheets/nanorolls obtained via fast and direct aqueous electrochemical exfoliation for high-capacity lithium storage, ACS Appl. Energy Mater. 6 (2023) 7180–7193.
[24] H.G. Oh, J.H. Na, S.-K. Park, Construction of mesoporous N-doped carbon-coated MXene-MoS_2 heterostructured microspheres via a spray-drying method as a high capacity and long cycle-life anode for potassium-ion batteries, J. Alloys Compd. 968 (2023) 171927.
[25] Q. Peng, F. Ling, H. Yang, P. Duan, R. Xu, Q. Wang, Y. Yu, Boosting potassium storage performance via construction of NbSe2–based misfit layered chalcogenides, Energy Storage Mater. 39 (2021) 265–270.
[26] A. Meerschaut, Misfit layer compounds, Curr. Opin. Solid State Mater. Sci. 1 (2) (1996) 250–259.
[27] A.G. Wiegers, Misfit layer compounds: structures and physical properties, Prog. Solid State Chem. 24 (1–2) (1996) 1–139.
[28] L. Zullo, G. Marini, T. Cren, M. Calandra, Misfit layer compounds as ultratunable field effect transistors: from charge transfer control to emergent superconductivity, Nano Lett. 23 (14) (2023) 6658–6663.
[29] A. Nader, A. Briggs, Y. Gotoh, Superconductivity in the misfit layer compounds (BiSe)1.10(NbSe2) and (BiS)1.11(NbS2), Solid State Commun. 101 (3) (1997) 149–153.
[30] M.F. Maqsood, U. Latif, Z.A. Sheikh, M. Abubakr, S. Rehman, K. Khan, M.A. Khan, H. Kim, M. Ouladsmane, M.A. Rehman, A comprehensive study of $Bi_2Sr_2Co_2O_y$ misfit layered oxide as a supercapacitor electrode material, Inorg. Chem. Commun. 158 (2023) 111487.
[31] X. Chen, H. Zhou, A. Kiswandhi, I. Miotkowski, Y. Chen, P. Sharma, A. Lima Sharma, M. Hekmaty, D. Smirnov, Z. Jiang, Thermal expansion coefficients of Bi_2Se_3 and Sb_2Te_3 crystals from 10 K to 270 K, Appl. Phys. Lett. 99 (26) (2011).
[32] F. Givens, G. Fredericks, Thermal expansion op $NbSe_2$ and TaS_2, J. Phys. Chem. Solid 38 (12) (1977) 1363–1365.
[33] K.-T. Chen, S. Chong, L. Yuan, Y.-C. Yang, H.-Y. Tuan, Conversion-alloying dual mechanism anode: Nitrogen-doped carbon-coated Bi_2Se_3 wrapped with graphene for superior potassium-ion storage, Energy Storage Mater. 39 (2021) 239–249.
[34] Z. Lv, H. Xu, W. Xu, B. Peng, C. Zhao, M. Xie, X. Lv, Y. Gao, K. Hu, Y. Fang, Quasi-topological intercalation mechanism of Bi0. 67NbS2 enabling 100 C fast-charging for sodium-ion batteries, Adv Energy Mater. (2023) 2300790.
[35] W.-C. Lin, Y.-C. Yang, H.-Y. Tuan, Ternary chalcogenide anodes for high-performance potassium-ion batteries and hybrid capacitors via composition-mediated bond softening and intermediate phase, Energy Storage Mater. 51 (2022) 38–53.
[36] M.E. Kamminga, M. Batuk, J. Hadermann, S.J. Clarke, Misfit phase (BiSe) 1.10NbSe2 as the origin of superconductivity in niobium-doped bismuth selenide, Commun. Mater. 1 (1) (2020) 82.
[37] W. Zhou, A. Meetsma, J. De Boer, G. Wiegers, Characterization and electrical transport properties of the misfit layer compounds (BiSe)1.10NbSe2 and (BiSe) 1.09TaSe2, Mater. Res. Bull. 27 (5) (1992) 563–572.
[38] X. Liu, Y. Sun, Y. Tong, H. Li, Unique spindle-like bismuth-based composite toward ultrafast potassium storage, Small 18 (44) (2022) 2204045.
[39] D.K. Ojha, R. Chatterjee, Y.-L. Lin, Y.-H. Wu, Y.-C. Tseng, Spin-torque efficiency enhanced in sputtered topological insulator by interface engineering, J. Magn. Magn. Mater. 572 (2023) 170638.
[40] Y.-Y. Hsieh, H.-Y. Tuan, Architectural van der Waals Bi2S3/Bi2Se3 topological heterostructure as a superior potassium-ion storage material, Energy Storage Mater. 51 (2022) 789–805.
[41] H.M. Ahmad, S. Ghosh, G. Dutta, A.G. Maddaus, J.G. Tsavalas, S. Hollen, E. Song, Effects of impurities on the electrochemical characterization of liquid-phase exfoliated niobium diselenide nanosheets, J. Phys. Chem. C 123 (14) (2019) 8671–8680.

[42] S. Naik, S. Kalaiarasan, R.C. Nath, S.N. Sarangi, A.K. Sahu, D. Samal, H.S. Biswal, S. L. Samal, Nominal effect of Mg intercalation on the superconducting properties of 2H–$NbSe_2$, Inorg. Chem. 60 (7) (2021) 4588–4598.
[43] H. Park, J.Y. Kim, J.Y. Oh, T.I. Lee, Long-term stable $NbSe_2$ nanosheet aqueous ink for printable electronics, Appl. Surf. Sci. 504 (2020) 144342.
[44] Z. Li, J. Yang, Z. Zhou, C. Mao, Z. Li, G. Li, Z. Zhang, Growth confinement and ion transportation acceleration via an in-situ formed Bi_4Se_3 layer for potassium ion battery anodes, Appl. Surf. Sci. 621 (2023) 156785.
[45] Q.H. Nguyen, H. Kim, I.T. Kim, W. Choi, J. Hur, Few-layer $NbSe_2$@ graphene heterostructures as anodes in lithium-ion half-and full-cell batteries, Chem. Eng. J. 382 (2020) 122981.
[46] C. Peng, H. Lyu, L. Wu, T. Xiong, F. Xiong, Z. Liu, Q. An, L. Mai, Lithium-and magnesium-storage mechanisms of novel hexagonal NbSe2, ACS Appl. Mater. Interfaces 10 (43) (2018) 36988–36995.
[47] J. Zhou, L. Wang, M. Yang, J. Wu, F. Chen, W. Huang, N. Han, H. Ye, F. Zhao, Y. Li, Hierarchical VS2 nanosheet assemblies: a universal host material for the reversible storage of alkali metal ions, Adv. Mater. 29 (35) (2017) 1702061.
[48] K. Cao, H. Liu, W. Li, Q. Han, Z. Zhang, K. Huang, Q. Jing, L. Jiao, CuO nanoplates for high-performance potassium-ion batteries, Small 15 (36) (2019) 1901775.
[49] Y. Wu, Y. Xu, Y. Li, P. Lyu, J. Wen, C. Zhang, M. Zhou, Y. Fang, H. Zhao, U. Kaiser, Unexpected intercalation-dominated potassium storage in WS 2 as a potassium-ion battery anode, Nano Res. 12 (2019) 2997–3002.
[50] C. Yang, J. Feng, F. Lv, J. Zhou, C. Lin, K. Wang, Y. Zhang, Y. Yang, W. Wang, J. Li, Metallic graphene-like VSe2 ultrathin nanosheets: superior potassium-ion storage and their working mechanism, Adv. Mater. 30 (27) (2018) 1800036.
[51] B. Xu, X. Ma, J. Tian, F. Zhao, Y. Liu, B. Wang, H. Yang, Y. Xia, Layer-structured $NbSe_2$ anode material for sodium-ion and potassium-ion batteries, Ionics 25 (2019) 4171–4177.
[52] Y. Luo, J. Han, Q. Ma, R. Zhan, Y. Zhang, Q. Xu, M. Xu, Exploration of NbSe2 flakes as reversible host materials for sodium-ion and potassium-ion batteries, ChemistrySelect 3 (34) (2018) 9807–9811.
[53] X. Liu, Y. Tong, Y. Wu, J. Zheng, Y. Sun, H. Li, In-depth mechanism understanding for potassium-ion batteries by electroanalytical methods and advanced in situ characterization techniques, Small Methods 5 (12) (2021) 2101130.
[54] X. Yang, A.L. Rogach, Electrochemical techniques in battery research: a tutorial for nonelectrochemists, Adv. Energy Mater. 9 (25) (2019) 1900747.
[55] J. Shi, L. Zu, H. Gao, G. Hu, Q. Zhang, Silicon-based self-assemblies for high volumetric capacity Li-ion batteries via effective stress management, Adv. Funct. Mater. 30 (35) (2020) 2002980.
[56] Z. Zhao, T. Xu, X. Yu, Unlock the potassium storage behavior of single-phased tungsten selenide nanorods via large cation insertion, Adv. Mater. 35 (5) (2023) 2208096.
[57] C.-H. Chang, K.-T. Chen, Y.-Y. Hsieh, C.-B. Chang, H.-Y. Tuan, Crystal facet and architecture engineering of metal oxide nanonetwork anodes for high-performance potassium ion batteries and hybrid capacitors, ACS Nano 16 (1) (2022) 1486–1501.